Numerical study of solar evaporation in 3D-printed structures

R Fillet, V Nicolas, Alain Celzard, Vanessa Fierro

Journal of Physics: Conference Series **2766** (2024) 012181 doi:10.1088/1742-6596/2766/1/012181

Numerical study of solar evaporation in 3D-printed structures

R Fillet[1], V Nicolas[1], A Celzard[1,2] and V Fierro[1]

[1]Université de Lorraine, CNRS, IJL, F-88000 Epinal, France
[2]Institut Universitaire de France (IUF), 75231 Paris, France

E-mail : vincent.nicolas@univ-lorraine.fr

Abstract. In this study, we used three-dimensional (3D) printed concave geometries filled with activated carbon to create a unique 3D solar evaporator for clean water production. The evaporation process was modeled considering airflow and solar radiation to investigate the advantages of 3D concave geometries. This work encompasses a series of studies, focusing on mass transfer inside the concavity and around the structure, to elucidate specific exchange points. Additionally, the research explores the effects of air velocity and the incorporation of additional holes within the structure, with the aim of improving evaporation.

Table 1. Nomenclature

c_p	heat capacity	J K^{-1} kg^{-1}	V_{in}	inflow velocity	m s^{-1}
D_{va}	diffusion coefficient of water vapor in air	m² s^{-2}	*Greek symbols*		
$\vec{g}$	gravitational constant	m s^{-2}	λ	thermal conductivity	W m^{-1} K^{-1}
h_c	thermal convection exchange coefficient	W m^{-2} K^{-1}	μ	dynamic viscosity	Pa s
h_v	vaporization enthalpy	kJ kg^{-1}	ρ	density	kg m^{-3}
H_r	relative humidity	%	c	concentration	kg m^{-3}
k_m	convective mass transfer coefficient	m.s^{-1}	*Subscripts and exponents*		
$\dot{m}$	evaporation rate	kg m^{-2} h^{-1}	*air*	ambient air	
M	molar mass	kg mol^{-1}	*i*	component i	
P	pressure	Pa	*m*	material	
P_s	average illumination on earth	W m^{-2}	*sat*	saturation	
R	universal gas constant	J mol^{-1} K^{-1}	*v*	vapor	
T	temperature	K	*w*	water	
$\vec{u}$	flow velocity	m s^{-1}	*0*	reference	

1. Introduction

As a result of global population growth, river pollution and global warming, it is estimated that by 2050, 3.9 billion people - over 40% of the world's population - will be living in water-stressed areas [1]. It is therefore necessary to develop new solutions for producing clean water using less energy. Solar energy is well suited to the production of clean water using an evaporation/condensation system [2]. By adding an evaporator material at the air/water interface, evaporation is considerably increased. The water vapor is then condensed on contact with a cold surface.

Water evaporation is a phenomenon that occurs at the interface between water, whether in liquid form or adsorbed on a surface, and the surrounding air. We have shown that the rate of water evaporation

depends on the air temperature around the evaporator material [3], while humidity also plays a role, but to a lesser extent. A higher air temperature also increases the saturation vapor pressure, thereby enabling the air to hold more water. In addition, the higher the interface temperature, the higher the local air temperature, which increases water evaporation. To improve evaporation efficiency, the material needs to exhibit high light absorption and retain heat at the interface [4,5]. Usually, an insulating foam is used to retain heat at the surface, over which the evaporator material is positioned under the solar flux. Water is pumped either through the material itself, or through cotton or another highly water-diffusive material. These materials can be made of metal or inorganic semiconductor nanostructures, polymers or carbon [6].

In a previous study, an original approach combining a carbon nanomaterial and 3D printing was used to study different types of geometries using experimental measurements and numerical modeling. The novelty of this approach was in the use of a 3D-printed structure coated with activated carbon (AC) powder as an evaporator material operating under convective flow. An investigation was conducted on a 2D flat surface and four different 3D structures to observe the phenomena associated with evaporation. The model was validated and simulation results presented.

Building on this previous research, the present study focuses on vapor transfers, using numerical simulation to analyze the impact of an open 3D structure functioning as a solar evaporator. Consequently, an analysis of mass exchange coefficients concerning all sides of the materials is carried out based on simulation results. Moreover, the effect of introducing additional perforations into a 3D paraboloid structure and the performance enhancement associated with increased air velocity is investigated.

2. Materials and methods

2.1. Evaporation material

Five geometries were studied: a 2D flat surface and four 3D structures, namely an inverted cone, a sphere and a paraboloid of revolution, with or without perforations. Detailed information about the materials can be found in a previous publication [7].

2.2. Numerical model

The solar simulator used in this study has an output power close to 1 kW. Several fans are used for cooling and induce an air flow around the structure, which is studied with a 3D model written using COMSOL Multiphysics 6.1. The model of the paraboloid evaporation material is shown in figure 1. In both the experimental setup and model configurations, the upper surface is exposed to solar radiation, cooled by convection with the air and evaporates water, as shown in figure 1a. Conversely, at the base, the process involves conduction only, with a fixed heat transfer coefficient.

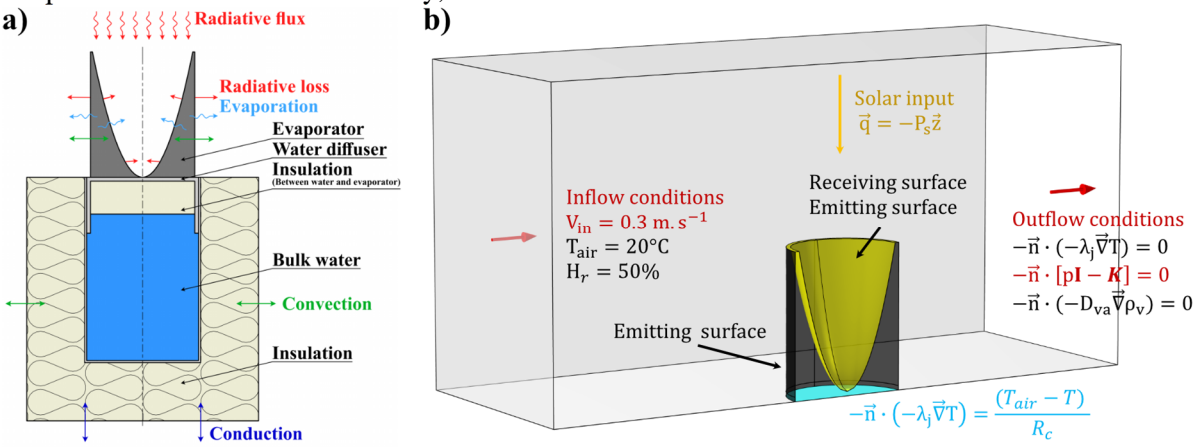

Figure 1. a) Schematic of the experimental evaporation system and associated physics; and b) schematic depicting the boundary conditions set in the simulation (only the computed section is shown here).

2.3. General equations

In order to simulate the heat and mass transfers existing during the evaporation process, the energy and mass conservation equations were used to obtain the temperature, T (Eq. 1), the fluid flow velocity, $\vec{u}$ (Eq. 2 and Eq. 3), and the vapor concentration in air, c_v (Eq. 5). The energy conservation equation accounts for conductive heat transfer and temperature changes over time. The heat transfer equation is therefore written as follows:

$$\rho_j c_{p,j} \vec{u} \cdot \vec{\nabla} T + \vec{\nabla} \cdot \left(-\lambda_j \vec{\nabla} T\right) = 0 \tag{1}$$

where ρ_j (kg m^{-3}) is the density, $c_{p,j}$ (J kg^{-1} K^{-1}) is the specific heat capacity, and λ_j (W m^{-1} K^{-1}) is the thermal conductivity of the component j (evaporator material, m, or air, a). The velocity of the fluid is described by the Navier-Stokes equations (Eq. 2) and the mass conservation equation (Eq. 3).

$$\rho_a \left(\vec{u} \cdot \vec{\nabla}\right) \vec{u} = \vec{\nabla} \cdot \left[-p\boldsymbol{I} + \mu(\nabla \vec{u} + (\nabla \vec{u})^T) - \frac{2}{3}\mu(\vec{\nabla} \cdot \vec{u})\boldsymbol{I}\right] - \rho_a \vec{g} \tag{2}$$

$$\vec{\nabla} \cdot (\rho_a \vec{u}) = 0 \tag{3}$$

where p (Pa) is the pressure, μ (Pa s) is the dynamic viscosity of air and $\vec{g}$ (m s^{-2}) is the gravitational constant of acceleration. ρ_a (kg m^{-3}) is the density of air and is calculated as follows in Eq. 4 :

$$\rho_a = \frac{pM_a}{RT} \tag{4}$$

where R (8.314 J mol^{-1} K^{-1}) is the universal gas constant and M_a (kg mol^{-1}) is the molar mass of air. Vapor transfer is described by the diffusion of water in air (Eq. 5):

$$\vec{\nabla} \cdot \left(\rho_v \vec{u} - D_{va} \vec{\nabla} \rho_v\right) = 0 \tag{5}$$

where D_{va} (m² s^{-1}) is the diffusion coefficient of vapor in air.

2.4. Boundary conditions

The boundary conditions used in the models are detailed in this section and shown in figure 1b. It should be noted that thermal continuity conditions are used in the heat equation (Eq. 1) for all internal boundaries.

Heat exchange at the surface takes into account convection, incoming light radiation and losses through water emission and evaporation (figure 1). Water evaporation involves the surface evaporation rate, $\dot{m}_{surf}$ (kg m^{-2} h^{-1}), multiplied by the energy required to raise the water temperature and the enthalpy of water vaporization, h_v (J kg^{-1}). For surface-to-surface radiation calculations, a specific set of equations from the COMSOL toolbox for surface-to-surface radiation is used. The solar energy source term, P_s (W m^{-2}), is defined so that solar energy is applied parallel to the material axis. At the upper surface, the diffusivity equation accounts for water loss, which corresponds to the evaporation rate. The surface of the material is assumed to be saturated with liquid water. Considering that water evaporation is due to the difference in mass concentration between the surface and air, $\dot{m}_{surf}$ is calculated as follows [8]:

$$\dot{m}_{surf} = -k_m \left(c_{v,sat} - c_v\right) \tag{6}$$

where k_m (m s^{-1}) is the convective mass exchange coefficient, and $c_{v,sat}$ (kg m^{-3}) is the vapor concentration at the air-material boundary, considered saturated.

For the sake of simplicity, heat conduction is represented as an overall thermal resistance, along with a fixed air temperature for the bottom part of the material boundary. During the experiment, the air flow velocity, V_{in}, was measured and found to be 0.3 m s^{-1}. This value and the air temperature T_{air} entering the domain, set at 293.15K, were used to calculate the water concentration. The remaining boundaries, shown in grey in figure 1b are also set to 20°C and 50% for T_{air} and H_r, respectively, and are considered as walls for flow physics. To reduce calculation time, a plane of symmetry passing through the center

of the structure in the direction of flow was used, allowing only half the geometry to be calculated. Figure 1b shows the calculated cross-section.

3. Results and discussion

3.1. Mass transfer of the different structures

Figure 2a shows the evaporation rate of the four structures studied in [7], serving as the basis for the current model. The structures are depicted along with their specific concavity and corresponding evaporation performance, represented by the evaporation rate. The results show a direct linear relationship between evaporation rate and total exchange area. Surprisingly, thermal convection was predominantly observed on the side of the cylinder rather than inside the concavity. Although the concavity was originally designed to capture radiation scattering, this particular effect appears to have a minimal impact on performance. To further investigate the importance of the concavity in solar evaporation, a study of the mass transfer coefficient k_m was conducted along the central axis of the geometry. The calculation of k_m was based on the balance of vapor flow at the boundary. Figure 2b shows the results, with the different shapes shown in the central graph. Each other graph, top, left and the right, shows the mass transfer coefficient along the geometry. Here, the left represents the FRONT of the geometry, while the right represents the REAR, considering that air flows from front to rear.

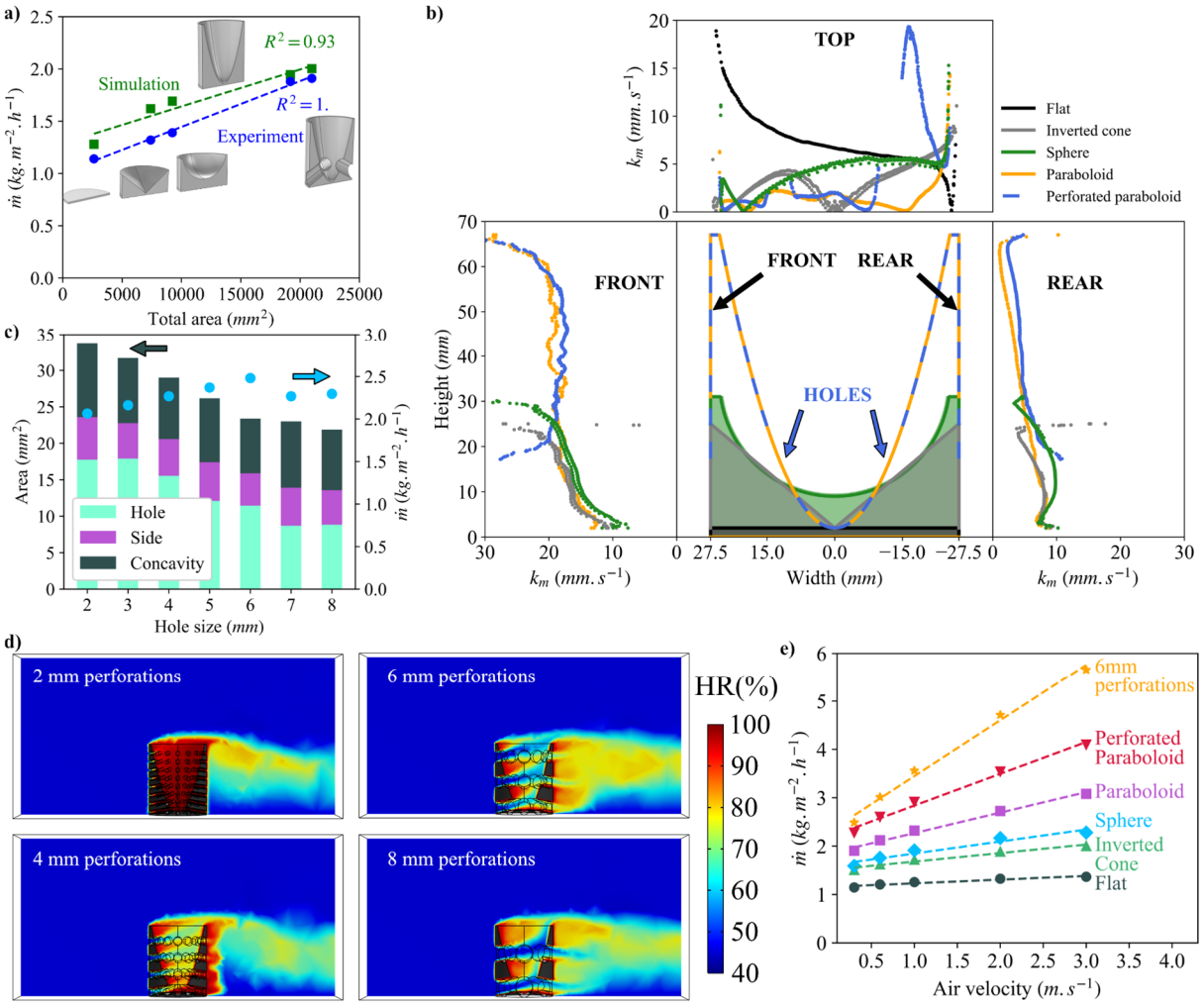

Figure 2 a) Experimental and simulated results of evaporation for the flat surface and the four 3D structures reproduced with permission from [7], Copyright 2023 Elsevier, b) mass transfer coefficient

calculated along the middle of the geometries for the front, rear and top, c) area of the different structures with perforations of different size and evaporation rate, d) relative humidity of four configurations with 2, 4, 6 and 8 mm perforations, and e) evaporation rate of the 5 initial cases and the 6mm perforation case for different air velocities.

The case of the 2D scenario, i.e., the flat surface, is shown only in the top graph of figure 2b, since there are no sides in this geometry. At the center of the flat disk, the transfer coefficient is around 7 mm s^{-1}. As air enters from the front, the coefficient peaks and then falls, probably due to boundary effects. However, concave shapes display a different behavior. Since the cylinder represents an obstacle for the air, mass transfer is higher at the rear of the concavity than at the front, as observed with the flat geometry. The inverted cone presents two distinct curves, with the front side showing curvature, while the rear side displays a linear trend with a minimum at the center and a maximum at the rear edge. In the sphere, mass transfer matches that of the flat disk at the rear, but decreases at the front. The paraboloid shows little mass transfer in its concavity, unlike the perforated paraboloid, where airflow through the perforations increases local mass transfer at the rear of the concavity. Notably, inside the concavities of the structures, mass transfers are limited, mainly due to the lack of airflow penetration, resulting in vapor-saturated air and obstructed transfers.
The behavior on the sides of the geometry, both front and rear, is similar for all structures. At the front, where the airflow touches the structure, the rate of mass transfer is the highest, reaching approximately 20 mm s^{-1} in a linear pattern. Conversely, at the rear, transfers are lower, with a minimum value at the top and a maximum at the bottom. This disparity can be attributed to vortex formation behind the structures, as reported in a previous study [7]. Overall, most exchanges occur on the sides of the geometry, contributing to the linear increase in total surface area shown in figure 2a. As the side of the structure increases, so does the total surface area, which improves evaporation. Inside the concavity, mass transfers are minimal. However, the use of a perforated paraboloid enhances mass transfer by allowing airflow to enter, facilitating the removal of water-saturated air and intensifying convection at the surface, thereby increasing mass transfers.

3.2. Performance enhancement through perforations of the structure

Since mass transfers are higher when perforations are made, a parametric study was conducted to explore the impact of different perforation sizes. Seven new perforated paraboloids were designed, each with an increasing perforation size, ranging from 2 mm to 8 mm in diameter. The perforations were arranged in the same way as depicted in the perforated paraboloid shown in figure 2a**,** with additional rows spaced by one diameter. In each case, the highest number of rows that could fit without altering the upper side of the concavity was used, resulting in a decreasing number of rows as the perforation diameter increased.
The structured varied as follows. The structure with 2 mm diameter holes (8 rows, 128 holes in total, 33709 m²) had the largest total area, while the structure with 8 mm diameter holes (2 rows, 16 holes in total, 21881 mm²) had the smallest total area. It is noteworthy that the area of the holes, i.e., the combined area of all the perforations, was greatest for the 3 mm structure and decreased as the diameter of the perforations increased. Figure 2c shows the different areas on the left-hand axis and the corresponding evaporation rates of the structures on the right-hand axis. Interestingly, contrary to the correlation seen in figure 2a between evaporation rate and total area, the best-performing structure had 6 mm perforations in 3 rows. For the structures with 7 and 8 mm perforations, only two rows were possible, which may explain why the evaporation rate did not increase further.
These results highlight the importance of surface exchange within 3D structures for solar evaporation, especially if air flow dynamics are considered. When forced convection is minimal, the capacity to remove saturated air, thereby enhancing mass transfer, outweighs the importance of the total area available for evaporation.

3.3. Performance increase with air velocity

The conditions simulating low forced convection were set to represent a gentle breeze resulting from the cooling of the solar simulator. Since additional perforations were found to be relevant for forced convection, a parametric study was conducted with all the structures from the initial study, including the paraboloid with 6 mm perforations, known for its superior performance. Air velocities of 0.3, 0.6, 1, 2, 3 m s^{-1} were set.

While the flat surface exhibited marginal improvements with increasing airflow, i.e., an increase of only 19% in evaporation rate from 0.3 m s^{-1} to 3 m s^{-1}, each 3D structure displayed a significant enhancement with increasing area. The inverted cone, sphere, paraboloid, and perforated paraboloid showed evaporation increases of 33%, 43%, 62% and 80%, respectively. This trend correlates with total area, a crucial factor driving the evaporation performance of concave structures. Notably, the open structure, specifically the one detailed in section 3.2 with 6 mm perforations, demonstrated the most substantial improvement, recording a 128% increase over the range of air velocities tested. At 0.3 m s^{-1}, its evaporation was very close to that of the structure with only a single row of perforations, but its performance increased significantly with higher air velocities, suggesting its potential effectiveness under conditions of high forced convection flow.

4. Conclusion

This study focuses on the evaporation performance of four 3D structures and a 2D flat case for reference. Previous findings established a linear relationship between evaporation rate and total area of evaporation under low convective flow conditions. The study of mass transfers inside the concavity and along the side revealed that most evaporation occurred on the cylindrical contour of the geometry. Additionally, the introduction of perforations proved effective in enhancing transfers inside the concavity by facilitating air flow and evacuating water-saturated air. Surprisingly, a parametric study on multiple perforations revealed an optimal result with 6 mm perforations, which did not match expectations based on the highest total area. Another investigation on air velocity indicated a direct correlation between surface exchange and performance improvement with increased velocity. Thus, the paraboloid with 6 mm perforations exhibited significant improvements, achieving a 127% increase when the velocity was multiplied tenfold. Overall, this study emphasizes the importance of open 3D structures to allow efficient airflow and thus enhance evaporation performance.

Acknowledgement

This work was partially supported by the French Ministry of the Armed Forces - Defence Innovation Agency - and TALiSMAN and TALiSMAN2 projects, funded by ERDF.

References

[1] Chen C, Kuang Y and Hu L 2019 Challenges and Opportunities for Solar Evaporation *Joule* **3** 683–718
[2] Fillet R, Nicolas V, Fierro V and Celzard A 2021 A review of natural materials for solar evaporation *Sol. Energy Mater. Sol. Cells* **219** 110814
[3] Fillet R, Nicolas V, Fierro V and Celzard A 2021 Modelling heat and mass transfer in solar evaporation systems *Int. J. Heat Mass Transf.* **181** 121852
[4] Zhang P, Liao Q, Yao H, Huang Y, Cheng H and Qu L 2019 Direct solar steam generation system for clean water production *Energy Storage Mater.* **18** 429–46
[5] Liu G, Xu J and Wang K 2017 Solar water evaporation by black photothermal sheets *Nano Energy* **41** 269–84
[6] Wu X, Chen G Y, Owens G, Chu D and Xu H 2019 Photothermal materials: A key platform enabling highly efficient water evaporation driven by solar energy *Mater. Today Energy* **12** 277–96
[7] Fillet R, Nicolas V, Celzard A and Fierro V 2023 Solar evaporation performance of 3D-printed concave structures filled with activated carbon under low convective flow *Chem. Eng*. J. **457** 141168
[8] Nicolas V, Vanin F, Grenier D, Lucas T, Doursat C and Flick D 2016 Modeling bread baking with focus on overall deformation and local porosity evolution *AIChE J.* **62** 3847–63